OPEN

Anti-escaping of incident laser in rare-earth doped fluoride ceramics with glass forming layer

H. F. Shi[1], P. J. Lin[2], J. X. Yang[1,3], J. L. Yuan[2], E. Y. B. Pun[3], Y. Song[1], X. Zhao[1]* & H. Lin[1,3]*

Adaptive fluoride ceramic with glass forming layer (GC_{ZBL}-Er) used in laser anti-escaping has been prepared by one-step synthesis, and the thickness of glass layer is identified as ~0.41 mm. Blue, green and red emissions of Er^{3+}/Yb^{3+} codoped fluoride ceramic (C_{ZBL}-Er) and glass layer (G_{ZBL}-Er) have been investigated under ~980 nm laser pumping. With the forming of thin glass layer on ceramic surface, the absorption intensities on diffuse reflection of GC_{ZBL}-Er at 974 nm and 1.53 μm increase by 48% and 53% than those of C_{ZBL}-Er. Excited by a 979 nm laser, the presence of the glass layer increases the absolute absorption rate in spectral power from 75% in C_{ZBL}-Er to 83% in GC_{ZBL}-Er, which is consistent with the improvement in the absorbed photon number. In addition, the quantum yield of GC_{ZBL}-Er complex is raised by 28.4% compared to the case of ceramic substrate by photon quantification. Intense absorption-conversion ability and efficient macroscopical anti-escaping effect confirm the superiority of ingenious structure in the fluoride ceramics with glass forming layer, which provides a new approach for developing the absorption-conversion materials of anti-NIR laser detection.

With the development of modern optical technology, the laser device has been widely employed in material processing, laser designator, medical diagnosis and other fields[1–3]. Nowadays, the laser beams applied in optical communication and laser ranging include the 1.54 μm erbium (Er^{3+}) doped glass laser and 980 nm high-power semiconductor laser[4–17]. Detection laser devices operate by two principles, one of which is to irradiate the laser beam on the attack target directly, such as laser blinding equipment, and then the other is to emit laser to the target and further receive the reflected wave, including ranging and semi-active laser guidance[18–22]. As the generation of laser equipment makes laser a threat for human heathy, the development of laser protection receives sustained attention. Absorptive typed laser-protective materials have been accredited as excellent candidates due to their wide applicability and convenient preparation[23–27]. On this basis, it is necessary to take some measures to greatly attenuate the intensity of the laser beam to achieve laser anti-escaping, which makes it better for anti-NIR laser detecting.

Rare earth (RE) elements possess unfilled 4 f electron layer structure, which produces a variety of energy levels, determining that RE ions doped materials can absorb photons of different wavelengths[28–41]. Among multitudinous RE ions, the level structure of Er^{3+} is rich and uniform, and Er^{3+} has strong absorption capacity in the ~980 nm and ~1.53 μm ranges commonly used in laser detection[42–50]. In addition, Yb^{3+} ion as sensitized ion can further absorb the NIR radiation efficiently and transfer the excitation energy to Er^{3+} via energy transfer processes, which can achieve large NIR laser absorption and efficient up-conversion emission, presenting a great potential in laser protection materials[51–59]. At present, the glass matrix typed laser protective material can overcome the shortcomings of the poor heat resistance, easy aging and low chemical resistance of the plastic matrix typed. However, the absorption ability of the general glass matrix typed material to laser is difficult to meet the application of the anti-NIR laser detection. Therefore, the exploration focusing on a new-type compound material with excellent absorption-conversion ability and high heat resistance potential becomes urgent in the future.

In this work, enhanced typed fluoride ceramic with glass forming layer has been prepared by one-step synthesis, and the laser stealth and interference can be realized based on the principle of RE^{3+} absorption, light conversion and energy transfer for NIR detecting laser. The complex reflection process between the glass-ceramic transition region and glass layer promotes the continuous consumption of incident laser, which obviously

[1]School of Textile and Material Engineering, Dalian Polytechnic University, Dalian, 116034, P.R. China. [2]Faculty of Maritime and Transportation, Ningbo University, Ningbo, 315832, P.R. China. [3]Department of Electronic Engineering and State Key Laboratory of Terahertz and Millimeter Waves, City University of Hong Kong, Tat Chee Avenue, Kowloon, Hong Kong, P.R. China. *email: zhaoxin@dlpu.edu.cn; lhai8686@yahoo.com
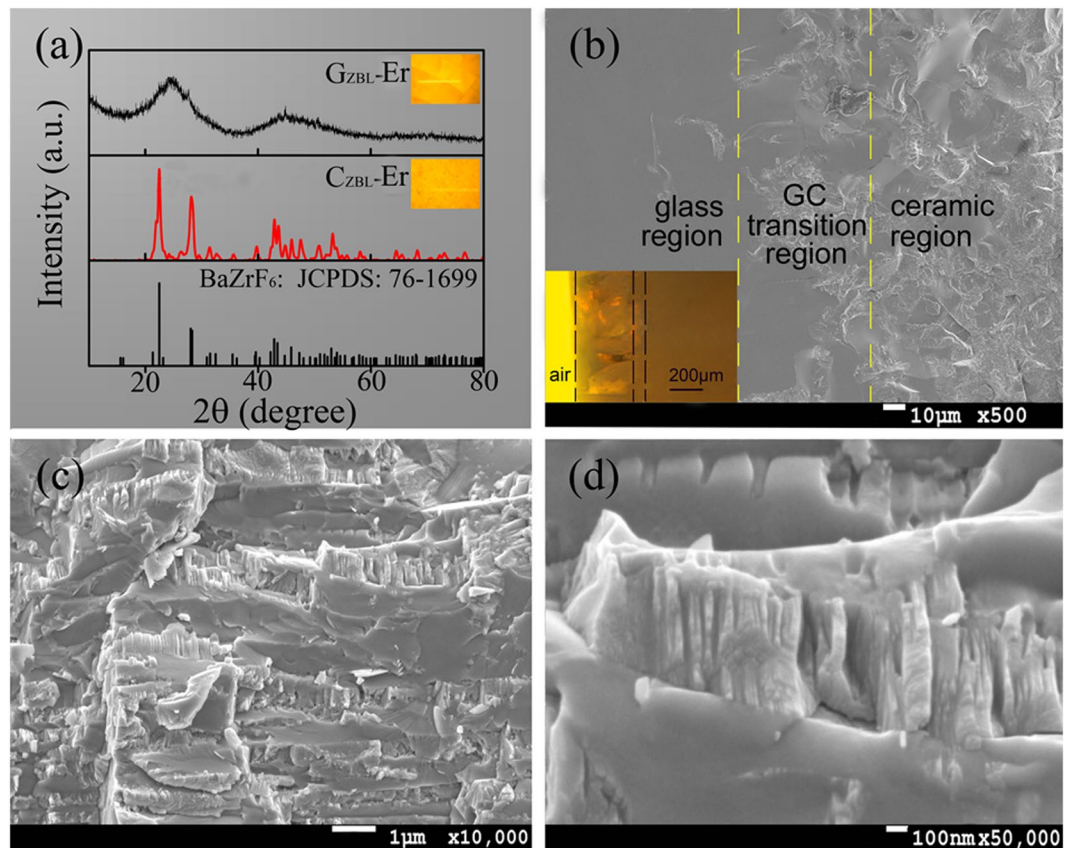
Figure 1. **(a)** XRD patterns of G$_{ZBL}$-Er and C$_{ZBL}$-Er powders. SEM images of **(b)** the glass-ceramic transition region and **(c,d)** the ceramic region of GC$_{ZBL}$-Er. Inset: Corresponding photographys under fluorescence microscope.

improves the absorption efficiency of the G$_{ZBL}$-Er. Here, the statement "anti-escape" is used to describe the material good absorption effect for incident laser light. In particular, the laser signals detected and tracked at 980 nm and 1.53 μm are strongly absorbed and converted into other wavelength light radiations. These results confirm that the special structure of fluoride ceramic equipped with glass layer can enhance absorption-conversion efficiency and laser anti-escaping effect for incident NIR rader laser.

Discussion

Structure and morphology property. To reveal absorption-conversion efficiency for NIR detecting laser, 1.0 wt% ErF$_3$ and 2.0 wt% YbF$_3$ as dopants are introduced into fluorozirconate matrix and denoted as GC$_{ZBL}$-Er, and individual glass and ceramic phase are labeled as G$_{ZBL}$-Er and C$_{ZBL}$-Er, respectively. XRD pattern of as-synthesized G$_{ZBL}$-Er powder exhibits a broad diffuse scattering at lower angles rather than the narrow diffraction peaks for crystal phase, and the amorphous nature of the G$_{ZBL}$-Er glass layer is well identified, as exhibited in Fig. 1(a). In addition, the detected diffraction peaks of C$_{ZBL}$-Er are in accordance well with the standard BaZrF$_6$ (JCPDS 76–1699), and the derived cell parameters (a = 7.744 Å, b = 11.691 Å, c = 5.404 Å, α = β = γ = 90°) of C$_{ZBL}$-Er are coincide with those of BaZrF$_6$ phase (a = 7.681 Å, b = 11.357 Å, c = 5.511 Å, α = β = γ = 90°), indicating the formation of the pure BaZrF$_6$ phase in upper layer of GC$_{ZBL}$-Er composite. Meanwhile, a little difference in cell parameters is attributed to the crystalline environment variation and the lattice deformation with the introduction of Er^{3+} and Yb^{3+} ions to some extent.

The microstructure and morphology of as-synthesized GC$_{ZBL}$-Er composite is explored, and the SEM image of the glass-ceramic transition region is displayed in Fig. 1(b). The interface between the glass and ceramic phase is obvious and uniform, and the thickness of the glass layer is measured to be ∼0.41 mm under the optical microscope. In addition, the grain size of the ceramics phase in Fig. 1(c,d) is identified to be 550 × 120 nm, and the crystalline phase of the rectangular structure with neat arrangement is further judged as the aggregation of several BaZrF$_6$ crystallites.

Under 980 nm laser excitation, the emission spectra of G$_{ZBL}$-Er and C$_{ZBL}$-Er powders with sundry pumping powers are depicted in Fig. 2(a,b), and four emission bands centered at 408, 522, 544 and 653 nm are attributed to f-f transitions $^2H_{9/2} \rightarrow {}^4I_{15/2}$, $^2H_{11/2} \rightarrow {}^4I_{15/2}$, $^4S_{3/2} \rightarrow {}^4I_{15/2}$ and $^4F_{9/2} \rightarrow {}^4I_{15/2}$, respectively. As the excitation power increases, the intensity of each peak increases exponentially, and the upconversion emission intensity I_{lumin} is proportional to the nth power of the 980 nm excitation intensity I_{excit}, which can be simply expressed as $I_{lumin} \propto I_{excit}^n$, where I_{lumin} is fluorescence intensity, I_{excit} is excitation power and n is the number of 980 nm photons absorbed per visible photon emitted. In addition, the intense upconversion green and red emissions are
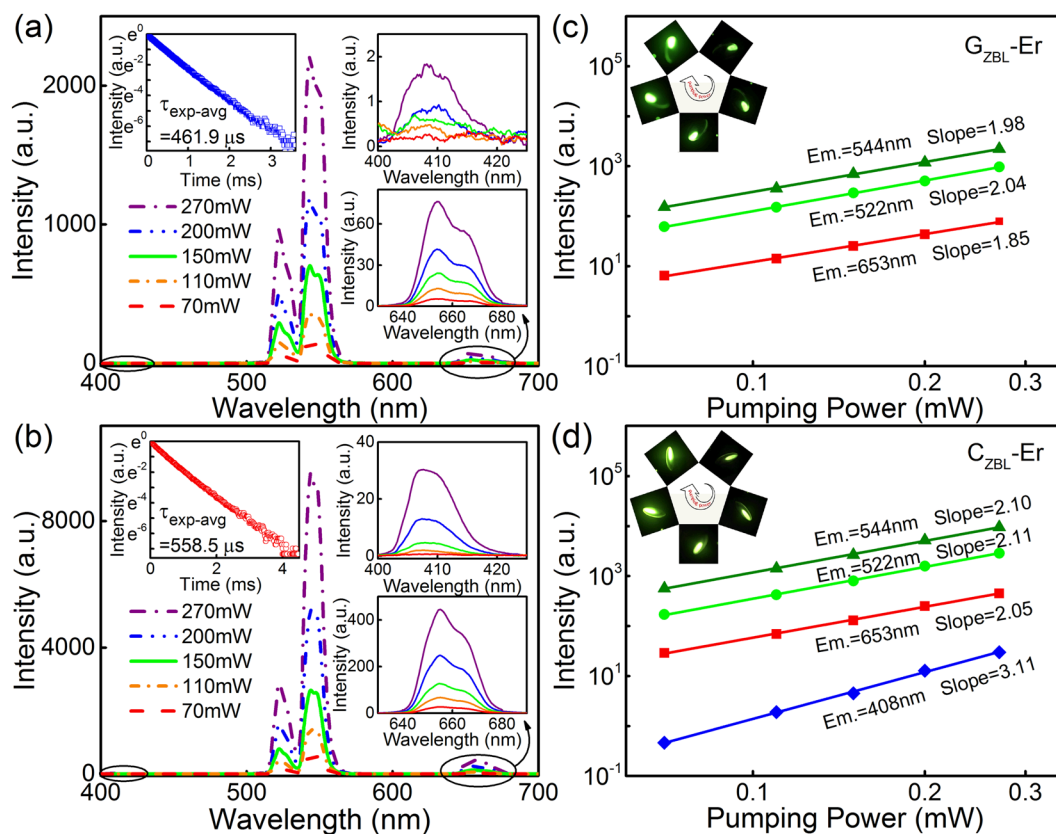
Figure 2. (a,b) Fluorescence emission spectra of G_{ZBL}-Er and C_{ZBL}-Er powders under 980 nm laser with various pumping powers. Inset: Corresponding fluorescence decay curves from the $^4S_{3/2}$ level of Er^{3+} in G_{ZBL}-Er and C_{ZBL}-Er monitored at 544 nm under the 487 nm excitation. (c,d) Dependence of emission intensities on excitation powers in G_{ZBL}-Er and C_{ZBL}-Er. Inset: Correlative fluorescent photographs with the increment of doping concentration in the clockwise direction.

confirmed to be two-photon absorption processes as indicated in Fig. 2(c,d), besides, rare 408 nm blue emission is identified as three-photon absorption process in the low phonon energy material.

In fluorozirconate glass system, the polyhedral network structure is formed mainly through Zr−F−Zr bridging, promoting the G_{ZBL}-Er sample with low phonon energy $\sim$570 cm^{-1} [60,61]. The characteristic can reduce the probability of non-radiative transition, which reflects intuitively in 544 nm emission of Er^{3+}. The fluorescence decay curves of the $^4S_{3/2}$ level for G_{ZBL}-Er and C_{ZBL}-Er layer monitored at 544 nm are exhibited in the inset of Fig. 2(a,b). In addition, the fluorescent lifetimes ($\tau_{exp\text{-}avg}$) of G_{ZBL}-Er and C_{ZBL}-Er are up to be 461.9 and 558.5 μs, respectively, which far exceed to 58 μs in $Li_2B_4O_7$ glass[62], 26 μs in SrF_2 nanocrystals[63], 333 μs in $NaYF_4$[64] and are close to 490 μs in oxyfluoride tellurite[65], indicating that the low phonon-energy material contributes to photon releasing effectively.

Enhanced absorption effect and principle analysis of GC$_{ZBL}$-Er. Although the optical transition capability of the glass fluorescent material to NIR laser are not as intense as crystal materials, when a glass forming layer is compounded on fluoride ceramics, the situation will be reversed. As exhibited in Fig. 3(a), the absorption intensities of GC$_{ZBL}$-Er at 974 and 1532 nm are $\sim$1.48 and $\sim$1.53 times higher than those in C_{ZBL}-Er, meanwhile. Correspondingly, the derived reflectance curve shown in Fig. 3(b) more clearly indicates that the reflectivity is reduced from 50% to 36% with the existence of thin glass layer. The reflected laser intensity including the Fresnel reflection is uniformly distributed and fully recorded in the integrating sphere, and the intensity radio of the reflected laser to incident laser can analyze the reflection ability of the material more macroscopically. Besides, the molar absorption coefficient α_{OH} can be used to evaluate the residual OH content in glass samples and is derived to be 0.91 cm^{-1} in 75TeO$_2$–10ZnO–10Na$_2$O–5GeO$_2$ glasses[66], while the value in this work glass is as low as 0.57 cm^{-1}. The FT-IR spectrum of glass layer is shown in Fig. 3(c), and the low OH content is beneficial for anticipated photon emitting of this material. The apparent improvement can be attributed to the complex surface morphology of ceramic matrix and the intense dispersion effect of glass layer, and the schematic diagram of the absorption mechanism is shown in Fig. 3(d). When the detection laser is incident into the composite material GC$_{ZBL}$-Er, it will be absorbed by the glass phase in the reflection process of the glass-ceramic transition region. Then the residual laser is re-reflected to the ceramic boundary owing to the specular effect of the glass layer, forming a multiple-cycle effect, which heightens the absorption ability effectively of GC$_{ZBL}$-Er for NIR laser. In addition, the interface of the glass to ceramic region in schematic diagram is a rough outline, while the actual
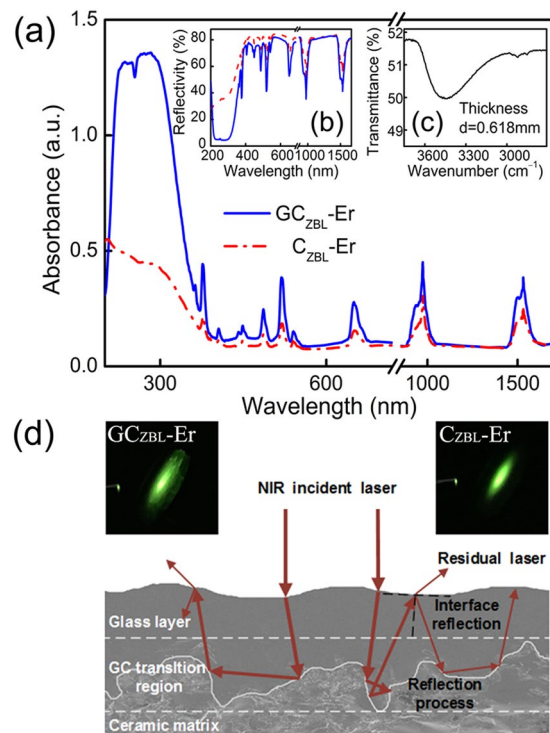
Figure 3. **(a)** Absorption spectra on diffuse reflection of C_{ZBL}-Er and GC_{ZBL}-Er samples. **(b)** Reflectivity spectra of C_{ZBL}-Er and GC_{ZBL}-Er. **(c)** FT-IR spectrum of glass layer. **(d)** Schematic diagram of GC_{ZBL}-Er absorption process under NIR incident laser. Inset: Fluorescent photographs of C_{ZBL}-Er and GC_{ZBL}-Er under 980 nm laser pumping.

surface topography is more complicated in fact. So the absorption effect of NIR incident laser is greatly increased with the complexity of the reflection process in the GC_{ZBL}-Er composite material. Just as the inset of Fig. 3(d), the facula area of GC_{ZBL}-Er is bigger than C_{ZBL}-Er and the luminous intensity is brighter at the same condition, showing that the GC_{ZBL}-Er composite increases the absorption intensity effectively to the NIR incident laser with the forming of thin glass layer on ceramic surface. Besides, the surface of formed glass is quietly smooth and further can effectively solve the follow-up cleaning problems in application. These results indicate that the complex structure of GC_{ZBL}-Er can be employed to enhance the absorption efficiency of $\sim$980 nm and $\sim$1.53 μm wavelengths, further exhibiting a laser anti-escaping effect.

Photon quantification on absorption-conversion potential *of* C_{ZBL}-Er and GC_{ZBL}-Er. In order to quantitatively characterize on absorption-conversion behavior of C_{ZBL}-Er and GC_{ZBL}-Er for laser beam, integrating sphere coupled with a CCD detector is applied to measure the absolute spectral parameters, which provides external quantum yield (QY) to evaluate luminescence and laser materials. Figure 4 presents the spectral power distributions as a function of 979 nm laser pumping power in C_{ZBL}-Er and GC_{ZBL}-Er samples, and the measured excitation powers are selected as 33, 106, 264, 400, 549 and 701 mW, respectively. Here, to ensure the laser fully diverged in integrating sphere, each sample is placed obliquely at the same angle and keeps a distance from the laser head. Besides, the tilt angle of the sample, the divergence angle of the laser and the distance of the laser head to the sample are measured to derive the area of the laser spot. Based on the above, the laser excitation power densities of the sample are further determined to be 16, 52, 129, 196, 269 and 344 mW/mm^2, respectively. Taking the high-power 701 mW and low-power 106 mW incident laser as an example, the 980 nm incident laser, the residual lasers on the excited glass surface and ceramic surface are measured as shown in Fig. 5. Furthermore, the absorption ratio of C_{ZBL}-Er to the incident laser is as high as 75.1% and 75.0% under 979 nm laser with 701 mW and 106 mW powers, respectively. Surprisingly, when the glass layer of GC_{ZBL}-Er sample faces laser head, the absorption rates further rise to 83.4% and 82.9%, which is attributed to the intense dispersion of laser beam between glass and ceramic, proving that the special structure of composite glass layer is more suitable for the absorption of NIR laser light.

As a clear resolution of the photon number cumulative conversion effect, the photon number distribution can further elaborate the up-conversion emission law of the sample. The photon quantization is adopted to explain the enhanced absorption-conservation ability and anti-escaping effect of glass layer to NIR lasers. Based on the net spectral power distribution, the photon number distribution can be derived by $N(\nu) = \frac{\lambda^3}{hc}P(\lambda)$, where λ is the wavelength, ν is the wavenumber, h is the Planck constant, c is the vacuum light velocity, and $P(\lambda)$ is spectral power distribution. The net absorption and emission photon distribution curves of C_{ZBL}-Er and GC_{ZBL}-Er are derived as presented in Fig. 6, and the integrated values are listed in Table 1. The green, red and NIR emissions at 522, 543, 665 and 848 nm are assigned to the $^2H_{11/2} \rightarrow {}^4I_{15/2}$, $^4S_{3/2} \rightarrow {}^4I_{15/2}$, $^4F_{9/2} \rightarrow {}^4I_{15/2}$ and $^4S_{3/2} \rightarrow {}^4I_{13/2}$ transitions
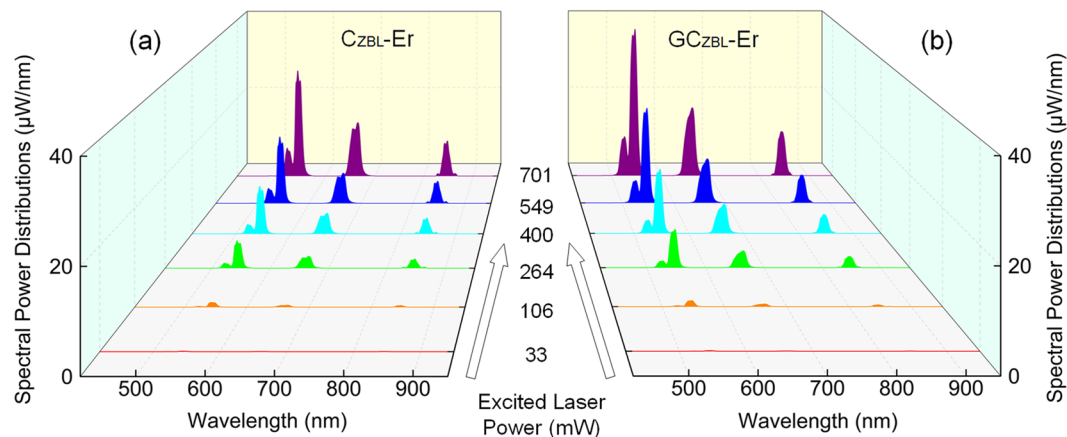
Figure 4. Net spectral power distributions of **(a)** C_{ZBL}-Er and **(b)** GC_{ZBL}-Er under the 979 nm laser excitation with different excitation powers.
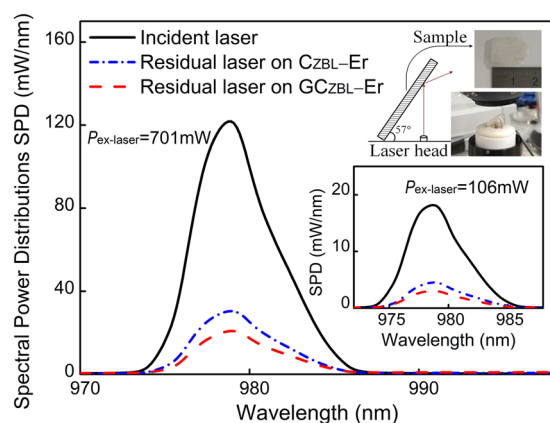
Figure 5. Spectral power distributions of the initial laser, the residual laser on C_{ZBL}-Er and GC_{ZBL}-Er under 701 mW and 106 mW laser powers in the integrating sphere. Inset: Location illustration of the sample measurement and the photograph of GC_{ZBL}-Er under natural light.

of Er^{3+}, respectively. In addition, the intense UC 848 nm emission is not easy to obtain, which provides more sufficient approaches for the conservation of incident laser. Since the ceramic substrate composites the glass layer, the emission intensity of GC_{ZBL}-Er at wavenumber is stronger than that in C_{ZBL}-Er material. When laser power density is selected to be 129 mW/mm², the net emission photons of four emissions at 522, 543, 665 and 848 nm are as high as 2.31×10^{14}, 11.49×10^{14}, 10.38×10^{14} and 6.62×10^{14} cps of C_{ZBL}-Er, respectively. Moreover, with the formation of the glass layer, emission photons further improve and reach to be 3.56×10^{14}, 16.48×10^{14}, 13.24×10^{14}, 8.75×10^{14} cps in GC_{ZBL}-Er, respectively. In addition, the enhanced percentage of total emitted photon number shows a trend of improving first and then decreasing slightly with the increase of laser pumping power. Figure 7(a,b) show the emission photon number of C_{ZBL}-Er and GC_{ZBL}-Er under the 979 nm laser with different excitation power density, where the rising tendency of the above four emission photons become dramatically severe, manifesting that the two-photon-excited luminescence has a positive dependency on the excitation power density.

The photoluminescence quantum yield (QY) is conducive to judge the luminous characters of optical materials, which provides a direct evaluation for the laser absorption-conversion efficiency. Thus the absolute fluorescence parameter of QY for C_{ZBL}-Er and GC_{ZBL}-Er are carried out based on $QY = N_{em}/N_{abs}$, where the N_{abs} and N_{em} represent the net absorption photon number and net emission photon number. The QYs for green, red and NIR UC emission of C_{ZBL}-Er and GC_{ZBL}-Er under 979 nm NIR laser with different pumping power densities are listed in Table 1 and illustrated in Fig. 7(c,d). As listed in Table 2, the total QYs of C_{ZBL}-Er and GC_{ZBL}-Er reach to be $0.86 \times 10^{-4} \sim 11.74 \times 10^{-4}$ and $0.96 \times 10^{-4} \sim 14.67 \times 10^{-4}$, respectively. The QY of the GC_{ZBL}-Er up to 7.96×10^{-4} is solved under the excitation of 129 mW/mm² power density, which is 28.4% more than that of C_{ZBL}-Er. The QYs of green and red emissions from Er^{3+} and Ho^{3+} in different glass matrices are listed in Table 3. As can be seen from the data, the high quantum yield in GC_{ZBL}-Er sample is over ten times higher than the values of BALMT glass, NMAG glass, BZYTLE glass and other oxide glasses[67–70]. However, the quantum yield in fluoride glass exceeds than that of GC_{ZBL}-Er[67], which is attributed to the superior absorption capacity of the composite with
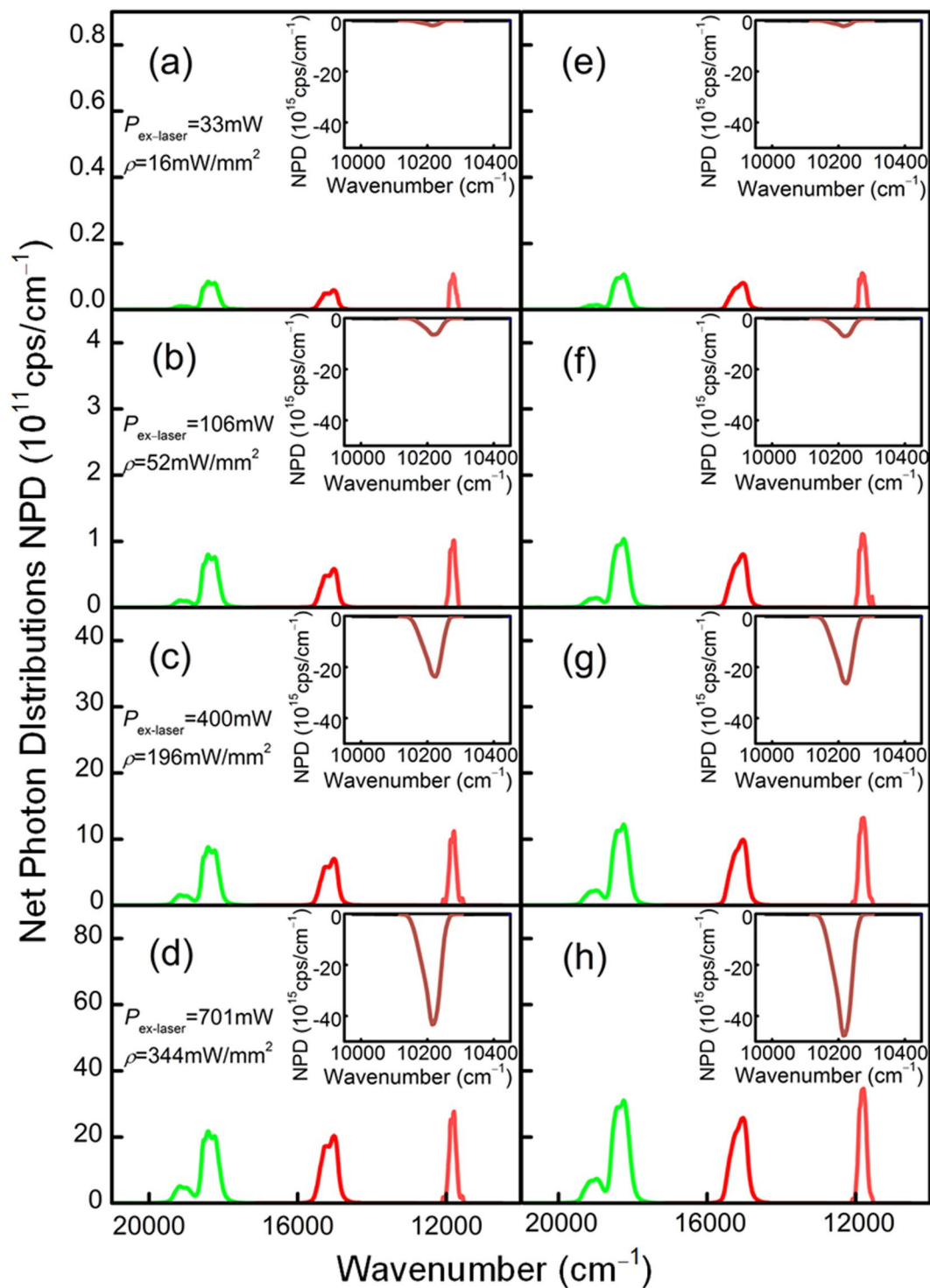
Figure 6. Net emission photon distributions in **(a–d)** C_{ZBL}-Er and **(e–h)** GC_{ZBL}-Er under the 979 nm laser excitation. Insets: details of related net absorption photon distributions of C_{ZBL}-Er and GC_{ZBL}-Er under the excitation of 979 nm laser in an integrating sphere.

special structure. With the enhancing incident laser power densities, the number of photons emitted increases exponentially, and the quantum yield improves continuously, which indicates that both absorption and emission of C_{ZBL}-Er and GC_{ZBL}-Er for NIR laser are still not saturated. Taken together, these results manifests that the forming of glass layer on ceramic substrate not only improves the absorption for NIR laser by the multi-reflection process, but also greatly enhances the optical-conversion ability, which confirms the GC_{ZBL}-Er complex processes a potential applied in anti-escaping of incident laser.

Excitation power density (mW/mm²)	Sample	Net absorption photon number (10¹⁶cps)	Enhanced percentage (%)	Emission photon number (10¹⁴cps)					Enhanced percentage (%)
				$^2H_{11/2} \rightarrow {}^4I_{15/2}$	$^4S_{3/2} \rightarrow {}^4I_{15/2}$	$^4F_{9/2} \rightarrow {}^4I_{15/2}$	$^4S_{3/2} \rightarrow {}^4I_{13/2}$	Total	
16	C_{ZBL}-Er	11.48	11.4	0.005	0.043	0.028	0.019	0.095	26.5
	GC_{ZBL}-Er	12.79		0.006	0.053	0.0392	0.022	0.120	
52	C_{ZBL}-Er	38.96	10.2	0.045	0.408	0.283	0.195	0.931	32.1
	GC_{ZBL}-Er	42.93		0.066	0.517	0.392	0.255	1.230	
129	C_{ZBL}-Er	97.05	9.9	0.338	2.458	1.890	1.332	6.018	41.0
	GC_{ZBL}-Er	106.67		0.502	3.484	2.668	1.830	8.484	
196	C_{ZBL}-Er	148.08	10.0	0.692	4.535	3.479	2.474	11.180	39.8
	GC_{ZBL}-Er	162.87		1.067	6.298	4.979	3.282	15.626	
269	C_{ZBL}-Er	205.03	8.6	1.435	7.750	6.356	4.423	19.964	38.4
	GC_{ZBL}-Er	222.76		2.152	10.954	8.734	5.791	27.631	
344	C_{ZBL}-Er	259.29	10.4	2.312	11.489	10.376	6.268	30.445	38.0
	GC_{ZBL}-Er	286.36		3.556	16.479	13.241	8.751	42.027	

Table 1. Absorption and emission photon numbers and enhanced percentage in the C_{ZBL}-Er and GC_{ZBL}-Er under the 979 nm laser excitation with different power densities.
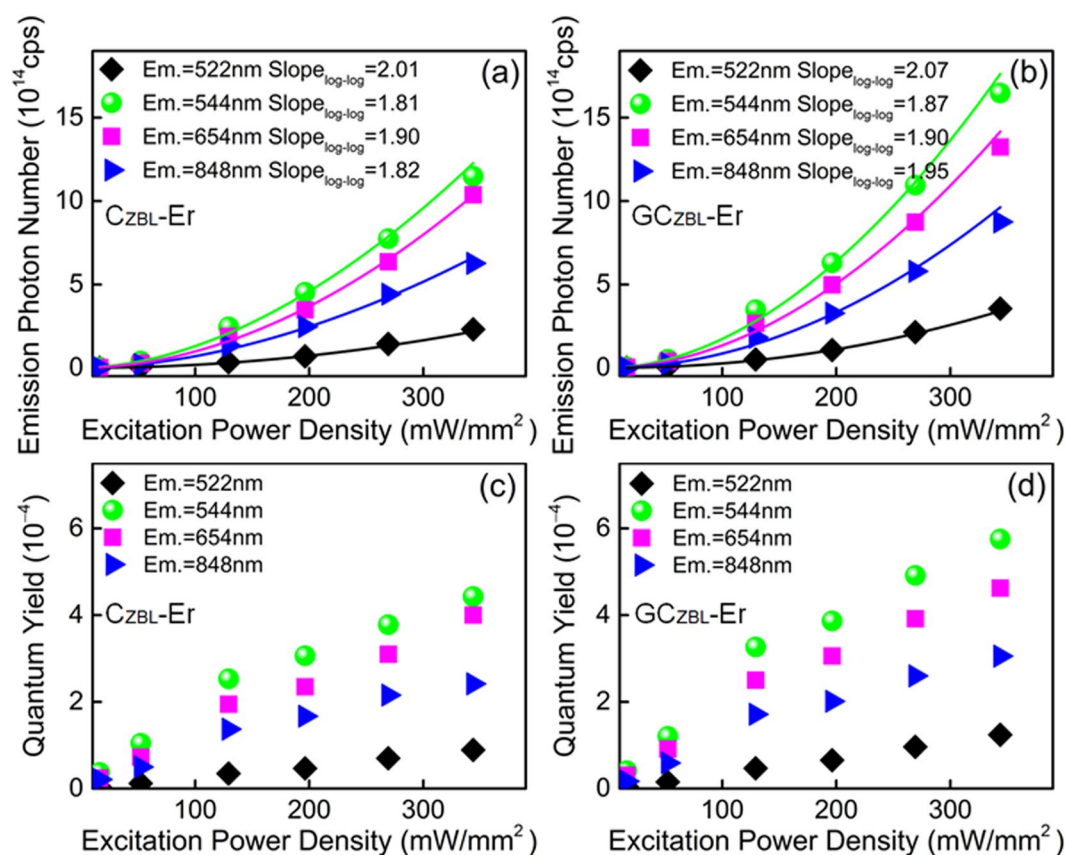
Figure 7. (a,b) Dependence of up-conversion emission photon numbers on excitation powers in C_{ZBL}-Er and GC_{ZBL}-Er. (c,d) Quantum yields of C_{ZBL}-Er and GC_{ZBL}-Er under the 979 nm laser with different excitation power density.

Conclusion

Multi-photon-excited blue, green, red and NIR emissions have been quantified in Er^{3+}/Yb^{3+} doped fluoride ceramic (C_{ZBL}-Er) and glass layer (G_{ZBL}-Er). The fluorescent lifetimes of G_{ZBL}-Er and C_{ZBL}-Er are up to be 461.9 and 558.5 μs, which indicates the fluorozirconate system can achieve effective photon releasing due to low maximum phonon energy. The absorption intensity of GC_{ZBL}-Er at 974 and 1532 nm are determined to be ∼1.48 and ∼1.53 times higher than those in C_{ZBL}-Er, and the absorption enhancement is attributed to the reflection of complex surface morphology on ceramic substrates and the diffusion absorption of glass layers. With the forming of

Excitation power density (mW/mm²)	Sample	Quantum yield (10^{-4})					Enhanced percentage (%)
		$^2H_{11/2} \to {}^4I_{15/2}$	$^4S_{3/2} \to {}^4I_{15/2}$	$^4F_{9/2} \to {}^4I_{15/2}$	$^4S_{3/2} \to {}^4I_{13/2}$	Total	
16	C_{ZBL}-Er	0.04	0.37	0.24	0.21	0.86	9.3
	GC_{ZBL}-Er	0.05	0.41	0.31	0.17	0.94	
52	C_{ZBL}-Er	0.12	1.05	0.73	0.50	2.40	14.6
	GC_{ZBL}-Er	0.15	1.20	0.91	0.59	2.85	
129	C_{ZBL}-Er	0.35	2.53	1.95	1.37	6.20	28.4
	GC_{ZBL}-Er	0.47	3.27	2.50	1.72	7.96	
196	C_{ZBL}-Er	0.47	3.06	2.35	1.67	7.55	27.3
	GC_{ZBL}-Er	0.66	3.87	3.06	2.02	9.61	
269	C_{ZBL}-Er	0.70	3.78	3.10	2.16	9.74	27.2
	GC_{ZBL}-Er	0.96	4.91	3.92	2.60	12.39	
344	C_{ZBL}-Er	0.89	4.43	4.00	2.42	11.74	25.0
	GC_{ZBL}-Er	1.24	5.75	4.62	3.06	14.67	

Table 2. Quantum yields of C_{ZBL}-Er and GC_{ZBL}-Er excited by the 979 nm laser.

Glasses	QY of green emission (~550 nm)	QY of red emission (~650 nm)	Experimental method	References
Er^{3+} doped silicate glass	2.0×10^{-7}	—	Relative method	[67]
Ho^{3+} doped NMAG	1.7×10^{-6}	24.1×10^{-6}	Absolute method	[68]
Er^{3+} doped NMAG	5.5×10^{-6}	21.9×10^{-6}	Absolute method	[68]
Er^{3+} doped BZYTLE (I)	2.3×10^{-5}	1.4×10^{-5}	Relative method	[69]
Er^{3+} doped BZYTLE (II)	3.3×10^{-5}	0.7×10^{-5}	Relative method	[69]
Ho^{3+} doped BALMT	6.3×10^{-5}	8.9×10^{-5}	Absolute method	[70]
Er^{3+} doped fluoride glasses	1.0×10^{-3}	—	Relative method	[67]
Er^{3+} doped C_{ZBL}	4.4×10^{-4}	4.0×10^{-4}	Absolute method	[This work]
Er^{3+} doped GC_{ZBL}	5.8×10^{-4}	4.6×10^{-4}	Absolute method	[This work]

Table 3. Comparison of quantum yields for green and red emissions from Ho^{3+} and Er^{3+} in various glasses.

thin glass film on ceramic surface, net absorption power and net absorption photon number of GC_{ZBL}-Er exhibit an increase of ~10% by photon quantization in the integrating sphere. Corresponding the emission photon number and quantum yield enhance by 40% and 28%, respectively, and the higher photon release efficiency further implies the superiority of the special composite structure in light conversion. The high absorption-conversation efficiency attributed to the complex structure of transition layer confirms the macroscopical anti-escaping effect in GC_{ZBL}-Er, which provides a reliable approach for anti-NIR laser detection.

Methods

Prototype design and fabrication of C_{ZBL}-Er and GC_{ZBL}-Er.
The fluoride ceramic-based composite glass layers were prepared based on the molar host composition of $60ZrF_4-30BaF_2-10LaF_3$ (ZBL) via the melt-quench method in reducing atmosphere. In addition, 1.0 wt% ErF_3 and 2.0 wt% YbF_3 as dopants were introduced into ZBL matrix and denoted as GC_{ZBL}-Er, and the individual glass phase and ceramic phase were labeled as G_{ZBL}-Er and C_{ZBL}-Er, respectively. The high-purity fluoride raw materials were melted at 900 °C for 5 min in a platinum crucible, and then the molten glasses were poured into a metal mold in a dry air atmosphere. Here, the lower liquid contacting with aluminum plate rapidly formed an ultrathin glass layer owing to the process of efficient heat conduction, where the metal mold quickly was taken away a lot of heat. Correspondingly, the upper liquid itself provided the energy needed for glass crystallization, which greatly promoted the formation of crystals and the adhesion of glass layers. Subsequently, all samples were annealed at 260 °C for 2 h, and then cooled down slowly to room temperature inside the furnace. For optical measurements, the annealed samples were sliced into pieces and polished into pieces with parallel sides.

Measurement and characterization.
The amorphous nature of G_{ZBL}-Er and the crystal structure of C_{ZBL}-Er were identified utilizing a Shimadzu XRD-7000 diffractometer with Cu-Kα radiation ($\lambda = 1.5406$ Å) operated at 40 kV and 30 mA. The morphological behaviors for the section of GC_{ZBL}-Er were observed by a field-emission scanning electron microscope (SEM instrument, JEOL JSM-7800F). The transmittance spectra of glass were recorded by a Perkin-Elmer FTIR/NIR Spectrometer (FTIR). The thickness of the glass layer of the GC_{ZBL}-Er was measured by a fluorescence microscope (Imaging system CK-500). Visible fluorescence spectra and fluorescence decay curves were determined by a Hitachi F-7000 fluorescence spectrophotometer equipped with an R928 photomultiplier tube (PMT) as a detector and a commercial Xe-lamp as an excitation source. Diffuse reflectance spectra of samples were recorded by Shimadzu corporation UV3600 spectrophotometer, and

the NIR emission spectra were implemented under the 980 nm laser by an Ocean Optics NIR-Quest 2250 fiber spectrometer.

The absolute spectral parameters of C_{ZBL}-Er and GC_{ZBL}-Er samples were measured in an integrating sphere of 3.3 inch inner diameter (Labsphere), which was connected to an exciting 979 nm NIR laser source and a QE65000 CCD detector (Ocean Optics) with 400 μm-core and 600 μm-core optical fibers, respectively. A standard halogen lamp (Labsphere, SCL-050) was adopted to calibrate this measurement system, and the spectral power distributions were obtained through fitting the factory data based on the black body radiation law.

Data availability

All data regarding the work presented here is available upon reasonable request to the corresponding author.

References

1. Ye, R., James, D. K. & Tour, J. M. Laser-Induced Graphene: From Discovery to Translation. *Adv. Mater.* **31**, 1803621 (2019).
2. Bao, H. *et al*. Laser cavity-soliton microcombs. *Nat. Photonics.* **13**, 384 (2019).
3. Bevilacqua, P. C. & Assmann, S. M. Rna structure: a laser-focused view into cells. *Nat. Chem. Biol.* **14**, 200–201 (2018).
4. Xue, T. *et al*. High thermal stability and intense 2.71 μm emission in Er^{3+}-doped fluorotellurite glass modified by GaF_3. *Opt. Mater.* **75**, 367–372 (2018).
5. Zhang, M. *et al*. High-gain polymer optical waveguide amplifiers based on core-shell $NaYF_4/NaLuF_4$: Yb^{3+}, Er^{3+} NPs-PMMA covalent-linking nanocomposites. *Sci. Rep-UK.* **6**, 36729 (2016).
6. Qi, F. W. *et al*. Highly Er^{3+} doped fluorotellurite glass for 1.5 μm broadband amplification and 2.7 μm microchip laser applications. *J. Lumin.* **202**, 132–135 (2018).
7. Vijaya, N. *et al*. Optical characterization of Er^{3+}-doped zinc fluorophosphate glasses for optical temperature sensors. *Sensor. Actuan. B-Chem.* **186**, 156–164 (2013).
8. Lu, Y. *et al*. Er^{3+} doped germanate–tellurite glass for mid-infrared 2.7 μm fiber laser material. *J. Quant. Spectrosc. Ra.* **171**, 73–81 (2016).
9. Lourenço, M. A., Milošević, M. M., Gorin, A., Gwilliam, R. M. & Homewood, K. P. Super-enhancement of 1.54 μm emission from erbium codoped with oxygen in silicon-on-insulator. *Sci. Rep-UK.* **6**, 37501 (2016).
10. Wang, X. *et al*. Detecting the origin of luminescence in Er^{3+}-doped hexagonal $Na_{1.5}Gd_{1.5}F_6$ phosphors. *Opt. Lett.* **41**, 5314–5317 (2016).
11. Wang, Y., Huang, Y. Y., Wang, Y., Lyu, P. & Hamblin, M. R. Photobiomodulation of human adipose-derived stem cells using 810 nm and 980 nm lasers operates via different mechanisms of action. *BBA-Gen. Subjects.* **1861**, 441–449 (2017).
12. Zlobina, E. A., Kablukov, S. I., Skvortsov, M. I., Nemov, I. N. & Babin, S. A. 954 nm Raman fiber laser with multimode laser diode pumping. *Laser Phys. Lett.* **13**, 035102 (2016).
13. Yang, C. *et al*. Ultra compact kilohertz-linewidth high-power single-frequency laser based on Er^{3+}/Yb^{3+}-codoped phosphate fiber amplifier. *Appl. Phys. Express.* **6**, 022703 (2013).
14. Taccheo, S. *et al*. Single-frequency waveguide lasers and their design. *IEEE. ICTON.* **2009**(11), 1–4 (2009).
15. Pal, A. *et al*. Ytterbium-sensitized Thulium-doped fiber laser in the near-IR with 980 nm pumping. *Opt. Express.* **18**, 5068–5074 (2010).
16. Tikhomirov, V. K. *et al*. Fabrication and characterization of nanoscale, Er^{3+}-doped, ultratransparent oxy-fluoride glass ceramics. *Appl. Phys. Lett.* **81**, 1937–1939 (2002).
17. Péron, O., Duverger-Arfuso, C., Jestin, Y., Boulard, B. & Ferrari, M. Enhanced spectroscopic properties in Er^{3+}/Yb^{3+}-activated fluoride glass–ceramics planar waveguides. *Opt. Mater.* **31**, 1288–1291 (2009).
18. Williams, B. S. Terahertz quantum-cascade lasers. *Nat. Photonics.* **1**, 517 (2007).
19. Kosterev, A. A. & Tittel, F. K. Chemical sensors based on quantum cascade lasers. *IEEE. J. Quantum Elect.* **38**, 582–591 (2002).
20. Williams, J. G., Turyshev, S. G. & Boggs, D. H. Lunar laser ranging tests of the equivalence principle. *Classical Quant. Grav.* **29**, 184004 (2012).
21. Sun, W., Yang, X., Yu, M., Wang, L. & Zhang, Q. Experimental and theoretical studies on the stable synthesis of a laser protective coating material erbium oxysulfide. *J. Mater. Sci-Mater. El.* **29**, 2406–2415 (2018).
22. Mariño- López, A. *et al*. Laser-protective soft contact lenses: Keeping an eye on the eye through plasmonics. *Appl. Mater. Today.* **15**, 1–5 (2019).
23. Feng, X. *et al*. Effect of the protective materials and water on the repairing quality of nickel aluminum bronze during underwater wet laser repairing. *Opt. Laser Technol.* **114**, 140–145 (2019).
24. Guo, C., Yin, S., Huang, L. & Sato, T. Synthesis of one-dimensional potassium tungsten bronze with excellent near-infrared absorption property. *ACS Appl. Mater. Inter.* **3**, 2794–2799 (2011).
25. Llordés, A., Garcia, G., Gazquez, J. & Milliron, D. J. Tunable near-infrared and visible-light transmittance in nanocrystal-in-glass composites. *Nature.* **500**, 323 (2013).
26. Adachi, K., Miratsu, M. & Asahi, T. Absorption and scattering of near-infrared light by dispersed lanthanum hexaboride nanoparticles for solar control filters. *J. Mater. Res.* **25**, 510–521 (2010).
27. de Pablos-Martin, A., Ferrari, M., Pascual, M. J. & Righini, G. C. Glass-ceramics: A class of nanostructured materials for photonics. *La Rivista del Nuovo Cimento.* **38**, 311–369 (2015).
28. Liu, Z. *et al*. Fabrication and characterization of mid-infrared emission of Pr^{3+} doped selenide chalcogenide glasses and fibres. *Rsc Adv.* **7**, 41520–41526 (2017).
29. Zhao, S. *et al*. The influence of phase evolution on optical properties in rare earth doped glass ceramics containing $NaYF_4$ nanocrystals. *J. Eur. Ceram. Soc.* **35**, 4225–4231 (2015).
30. Zhang, J., Song, F., Lin, S., Liu, S. & Liu, Y. Tunable fluorescence lifetime of Eu-PMMA films with plasmonic nanostructures for multiplexing. *Opt. Express.* **24**, 8228–8236 (2016).
31. Zhu, Z., Fu, G., Yang, Y., Yang, Z. & Li, P. Tunable luminescence and energy transfer properties in $Na_3Bi(PO_4)_2$: Eu^{3+}, Tb^{3+}, Dy^{3+}, Sm^{3+} phosphors with high thermal stability. *J. Lumin.* **184**, 96–109 (2017).
32. Rafiei Miandashti, A., Khosravi Khorashad, L., Govorov, A. O., Kordesch, M. E. & Richardson, H. H. Time-Resolved Temperature-jump measurements and theoretical simulations of nanoscale heat transfer using $NaYF_4$: Yb^{3+}: Er^{3+} upconverting nanoparticles. *J. Phys. Chem. C.* **123**, 3770–3780 (2019).
33. Viji, V. *et al*. Synthesis and luminescence characterization of $Sr_{0.5}Ca_{0.5}TiO_3$:Sm^{3+} phosphor. *Spectrochim. Acta A.* **150**, 419–429 (2015).
34. Cheng, X. *et al*. Er^{3+} sensitized photon upconversion nanocrystals. *Adv. Funct. Mater.* **28**, 1800208 (2018).
35. Rabouw, F. T. *et al*. Quenching pathways in $NaYF_4$: Er^{3+}, Yb^{3+} upconversion nanocrystals. *Acs nano.* **12**, 4812–4823 (2018).

36. Ishii, A. *et al.* Multicolor upconversion luminescence of dye-coordinated Er^{3+} at the interface of Er_2O_3 and CaF_2 nanoparticles. *Sci. Technol. Adv. Mat.* **20**, 44–50 (2019).
37. Taccheo, S. *et al.* Er: Yb-doped waveguide laser fabricated by femtosecond laser pulses. *Opt. Lett.* **29**, 2626–2628 (2004).
38. Quimby, R. S., Miniscalco, W. J. & Thompson, B. Clustering in erbium-doped silica glass fibers analyzed using 980 nm excited-state absorption. *J. Appl. Phys.* **76**, 4472–4478 (1994).
39. Mukhopadhyay, L., Rai, V. K., Bokolia, R. & Sreenivas, K. 980 nm excited $Er^{3+}/Yb^{3+}/Li^+/Ba^{2+}$: $NaZnPO_4$ upconverting phosphors in optical thermometry. *J. Lumin.* **187**, 368–377 (2017).
40. Rolli, R. *et al.* Yellow-to-blue frequency upconversion in Pr^{3+}-doped aluminium fluoride glasses. *J. Non-Cryst. Solids.* **280**, 269–276 (2001).
41. de Pablos-Martín, A. *et al.* Effects of Tm^{3+} Additions on the Crystallization of LaF_3 Nanocrystals in Oxyfluoride Glasses: Optical Characterization and Up-Conversion. *J. Am. Ceram. Soc.* **96**, 447–457 (2013).
42. Aidilibike, T., Guo, J., Li, Y., Liu, X. & Qin, W. Triplet cooperative luminescence of Yb^{3+}-doped AF_2, (A = Ca, Sr) crystals. *J. Lumin.* **188**, 107–111 (2017).
43. Qin, Y., Yang, Z., Yang, Y., Zhou, D. & Qiu, J. Multi-color tunable luminescence in Yb^{3+}, Er^{3+} codoped $NaYF_4$ nanocrystals based on size-dependent. *Sci. Adv. Mater.* **9**, 668–672 (2017).
44. Huang, S. *et al.* Multifunctional chitosan modified Gd_2O_3:Yb^{3+}, Er^{3+}@$nSiO_2$@$mSiO_2$ core/shell nanoparticles for pH responsive drug delivery and bioimaging. *Rsc Adv.* **7**, 10287–10294 (2017).
45. Sreeja, E., Gopi, S., Joseph, C., Unnikrishnan, N. V. & Biju, P. R. Structural and photoluminescence properties of UV-excited Er^{3+} doped Ba_2CaWO_6 yellowish-green phosphors. *Physica B.* **555**, 74–80 (2019).
46. Wang, Z. *et al.* Superlong and color-tunable red persistent luminescence and photostimulated luminescence properties of $NaCa_2GeO_4F$:Mn^{2+}, Yb^{3+} phosphor. *Inorganic Chemistry* **55**, 12822 (2016).
47. Grzyb, T. & Przybylska, D. Formation mechanism, structural, and upconversion properties of alkaline rare-earth fluoride nanocrystals doped with Yb^{3+}/Er^{3+} ions. *Inorg. Chem.* **57**, 6410–6420 (2018).
48. Man, S. Q., Pun, E. Y. B. & Chung, P. S. UC luminescence of Er^{3+} in alkali bismuth gallate glasses. *Appl. Phys. Lett.* **77**, 483–485 (2000).
49. Kir'yanov, A. V., Barmenkov, Y. O., Martinez, I. L., Kurkov, A. S. & Dianov, E. M. Cooperative luminescence and absorption in Ytterbium-doped silica fiber and the fiber nonlinear transmission coefficient at $\lambda = 980$ nm with a regard to the Ytterbium ion-pairs' effect. *Opt. Express.* **14**, 3981–3992 (2006).
50. Simpson, D. A. *et al.* Visible and near infra-red up-conversion in Tm^{3+}/Yb^{3+} co-doped silica fibers under 980 nm excitation. *Opt. Express.* **16**, 13781–13799 (2008).
51. Chen, Z. *et al.* Nonlinear negative transmittance at a CW 980-nm laser diodes pumping in Yb^{3+}: CaF_2 nanocrystals-embedded glass ceramics. *J. Am. Ceram. Soc.* **100**, 612–619 (2017).
52. Huang, F., Gao, Y., Zhou, J., Xu, J. & Wang, Y. Yb^{3+}/Er^{3+} co-doped $CaMoO_4$: a promising green upconversion phosphor for optical temperature sensing. *J. Alloy. Compd.* **639**, 325–329 (2015).
53. Gorni, G. *et al.* Effect of the heat treatment on the spectroscopic properties of Er^{3+}-Yb^{3+}-doped transparent oxyfluoride nano-glass-ceramics. *J. Lumin.* **193**, 51–60 (2018).
54. Zhou, D., Li, D., Zhou, X., Xu, W. & Song, H. Semiconductor plasmon induced upconversion enhancement in $mCu_{2-x}S$@SiO_2@Y_2O_3:Yb^{3+}, Er^{3+} core-shell nanocomposites. *Acs Appl. Mater Inter.* **9**, 35226 (2017).
55. Morassaei, M. S., Salehabadi, A., Akbari, A., Tavassoli, S. H. & Salavati-Niasari, M. Enhanced dye sensitized solar cells efficiency by utilization of an external layer of $CaCe_2 (MoO_4)_4$: Er^{3+}/Yb^{3+} nanoparticles. *J. Alloy. Compd.* **769**, 732–739 (2018).
56. Chen, Y., Chen, G. H., Liu, X. Y. & Yang, T. Enhanced up-conversion luminescence and optical thermometry characteristics of Er^{3+}/Yb^{3+} co-doped transparent phosphate glass-ceramics. *J. Lumin.* **195**, 314–320 (2018).
57. Venkatramu, V. *et al.* Optical properties of Yb^{3+} -doped phosphate laser glasses. *J. Alloy. Compd.* **509**, 5084–5089 (2011).
58. Pisarski, W., Pisarska, J., Lisiecki, R. & Ryba-Romanowski, W. Er^{3+}/Yb^{3+} co-doped lead germanate glasses for up-conversion luminescence temperature sensors. *Sensor. Actuat. B-Chem.* **252**, 54–58 (2016).
59. Kumar, C. A., Kumar, S. S., Dwivedi, A., Amresh, B. & Rai, S. B. Enhanced upconversion emission of Er^{3+}/Yb^{3+} and $Er^{3+}/Yb^{3+}/Zn^{2+}$ doped calcium aluminate for use in optical thermometry and laser induced optical heating. *Methods Appl. Fluores.* **6**, 035014 (2018).
60. Tian, Y., Wei, T., Jing, X., Zhang, J. & Xu, S. Enhanced 2.7-and 2.9-μm emissions in Er^{3+}/Ho^{3+} doped fluoride glasses sensitized by Pr^{3+} ions. *Mater. Res. Bull.* **76**, 67–71 (2016).
61. Wang, Y., Wang, S., Deng, S., Liu, J. & Zhang, J. Effect of the addition of MgF_2 and NaF on the thermal, optical and magnetic properties of fluoride glasses for sensing applications. *Opt. Mater.* **72**, 341–345 (2017).
62. Runowski, M. *et al.* Lifetime nanomanometry-high-pressure luminescence of up-converting lanthanide nanocrystals–SrF_2: Yb^{3+}, Er^{3+}. *Nanoscale.* **9**, 16030–16037 (2017).
63. Padlyak, B. V., Lisiecki, R. & Ryba-Romanowski, W. Spectroscopy of the Er-doped lithium tetraborate glasses. *Opt. Mater.* **54**, 126–133 (2016).
64. Wang, Y., Deng, R., Xie, X., Huang, L. & Liu, X. Nonlinear spectral and lifetime management in upconversion nanoparticles by controlling energy distribution. *Nanoscale.* **8**, 6666–6673 (2016).
65. Chen, F. *et al.* Investigation of mid-infrared emission characteristics and energy transfer dynamics in Er^{3+} doped oxyfluoride tellurite glass. *Sci. Rep-UK.* **5**, 10676 (2015).
66. Rivera, V. A. G., El-Amraoui, M., Ledemi, Y., Messaddeq, Y. & Marega, E. Jr. Expanding broadband emission in the near-IR via energy transfer between Er^{3+}-Tm^{3+} co-doped tellurite-glasses. *J. Lumin.* **145**, 787–792 (2014).
67. Quimby, R. S., Drexhage, M. G. & Suscavage, M. J. Efficient frequency up-conversion via energy transfer in fluoride glasses. *Electron. Lett.* **23**, 32–34 (1987).
68. Zhu, C. L., Pun, E. Y. B., Wang, Z. Q. & Lin, H. UC photon quantification of holmium and erbium ions in waveguide-adaptive germanate glasses. *Appl. Phys. B.* **123**, 64 (2017).
69. Yeh, D. C., Sibley, W. A., Suscavage, M. & Drexhage, M. G. Multiphonon relaxation and infrared-to-visible conversion of Er^{3+} and Yb^{3+} ions in barium-thorium fluoride glass. *J. Appl. Phys.* **62**, 266–275 (1987).
70. Li, B. R., Zhao, X., Pun, E. Y. B. & Lin, H. Upconversion photon quantification of Ho^{3+} in highly transparent fluorotellurite glasses. *Opt. Laser. Technol.* **107**, 8–14 (2018).

Acknowledgements

Author contributions

H.F. Shi and H. Lin conceived and designed the experiments. H.F. Shi, P.J. Lin and J.X. Yang carried out most of the experiments and data analysis. H.F. Shi, P.J. Lin, J.X. Yang, J.L. Yuan, E.Y.B. Pun, Y. Song, X. Zhao and H. Lin discussed the results and commented on the manuscript. H.F. Shi, P.J. Lin and J.X. Yang wrote and revised the manuscript.

Competing interests

The authors declare no competing interests.

Additional information

Correspondence and requests for materials should be addressed to X.Z. or H.L.

Reprints and permissions information is available at www.nature.com/reprints.

Publisher's note Springer Nature remains neutral with regard to jurisdictional claims in published maps and institutional affiliations.